PNAS NEXUS

PNAS Nexus, 2025, 4, pgaf109

https://doi.org/10.1093/pnasnexus/pgaf109
Advance access publication 7 April 2025
Research Report

Seasonally resolved stratigraphy at Jwalapuram India shows regional surface warming after the Toba volcanic super-eruption

Gopesh Jha[a,b,c,*], Mafalda Costa[b,d], Anna Tsoupra[b], Cristina Barrocas Dias[b,d,e], Ola Kwiecien[f], Jack Longman[f], Sebastian F. M. Breitenbach[f], Peter Ditchfield[g], Deepak Kumar Jha[h], Rachel Rudd[h], Devara Anil[i], Roshan Paladugu[j], Sindu Shree[k], Hema Achyuthan[l], Rachna Raj[m], K. Krishnan[i,*], Nicole Boivin[a,n,o,*], Patrick Roberts[a,h,*] and Michael Petraglia[o,p,q,*]

[a]Max Planck Institute of Geoanthropology, Jena 07745, Germany
[b]HERCULES laboratory, University of Évora, Évora H3CV+M5, Portugal
[c]Institute for Archaeological Sciences, Eberhard-Karls-Universität Tübingen, Tübingen 72070, Germany
[d]IN2PAST Associate Laboratory, University of Évora, Évora H3CV+M5, Portugal
[e]Department of Chemistry and Biochemistry, University of Évora, Évora H3CV+M5, Portugal
[f]Department of Geography and Environmental Sciences, Northumbria University, Newcastle-upon-Tyne NE1 8ST, United Kingdom
[g]School of Archaeology, University of Oxford, Oxford OX1 3TG, United Kingdom
[h]Department of Coevolution of Land Use and Urbanisation, Max Planck Institute of Geoanthropology, Jena 07745, Germany
[i]Department of Archaeology and Ancient History, The Maharaja Sayajirao University of Baroda, Vadodara 390002, India
[j]Department of Evolutionary Genetics, Max Planck Institute for Evolutionary Anthropology, Leipzig 04103, Germany
[k]Institute for Materials Science, Functional Nanomaterials, Kiel University, Kiel 24143, Germany
[l]Department of Geology, Anna University, Chennai 600025, India
[m]School of Environmental Sciences, Jawaharlal Nehru University, New Delhi 110067, India
[n]School of Environment and Science, Griffith University, Nathan, Brisbane, QLD 4111, Australia
[o]School of Social Science, University of Queensland, St Lucia, Brisbane, QLD 4072, Australia
[p]Human Origins Program, Smithsonian Institution, Washington, DC 20024, USA
[q]Australian Research Centre for Human Evolution, Griffith University, Nathan, Brisbane, QLD 4111, Australia
*To whom correspondence should be addressed: Email: gjha@gea.mpg.de (G.J.); Email: krishnan.msu@gmail.com (K.K.); Email: Boivin@gea.mpg.de (N.B.); Email: roberts@gea.mpg.de (P.R.); Email: m.petraglia@griffith.edu.au (M.P.)
Edited By Dennis Hartmann

Abstract

Understanding the nature and tempo of global environmental responses to the ~74,000 BP (~74 ka) Toba volcanic super-eruption is based primarily on historical analogies and climate models that lack ground-truthing in regions distal to eruptions. Here, we report the first proxy-based terrestrial record of the immediate environmental impact of the Younger Toba Tuff (YTT) eruption on the hominin-occupied ecosystem in peninsular India, spanning six annual monsoonal cycles directly following the YTT event. We present a multiproxy paleoclimate dataset from Jwalapuram in southern India, featuring a geochemical characterization of multiple YTT tephra and hardpan layers, complemented by detailed stratigraphic observations, sedimentological insights, and stable carbon isotope data. Taken together, these multiple lines of evidence show a progressive trend of tephra weathering and strong evapotranspiration in the immediate aftermath of the YTT, suggesting multiannual regional warming. Our results underline the complex responses of regional environments to the Toba super-eruption, which extend beyond a simple widespread "volcanic winter."

Keywords: Young Toba Tuff (YTT), short-term impact, climate change, Indian subcontinent, Indian summer monsoon (ISM)

Significance Statement

The ~74 ka Younger Toba Tuff (YTT) eruption has been argued to have had global climatic and environmental impacts, with ramifications for human evolution. This remains hotly debated, necessitating high-resolution paleoenvironmental reconstruction, particularly from hominin associated contexts. Our study presents the first multiproxy terrestrial paleoclimate record for peninsular India which documents short-term environmental responses to the YTT super-eruption. Our novel paleoclimate data do not show any signs of a dramatic "volcanic winter." Instead, they present evaporative conditions and surface warming which may have impacted regional ecosystems in more subtle, yet still significant ways. Our work underscores the necessity of on-site paleoclimate data when exploring YTT impacts at the human scale, contributing to a more nuanced understanding of ecological responses to massive volcanic eruptions.

Competing Interest: The authors declare no competing interests.
Received: February 3, 2025. **Accepted:** March 26, 2025

Introduction

Volcanic eruptions represent extreme phenomena with profound implications for climate dynamics, the biosphere, and human societies across varied spatial scales, ranging from the local to the global (1–3). As exemplified by historical tropical volcanic eruptions (TVEs), such as Krakatau, Tambora, Agung, and Pinatubo, the substantial release of aerosols during volcanic events induces upper atmospheric turbidity, with the resulting interception of solar radiation often triggering a cooling effect (also known as volcanic cooling or winter) (1–5). TVEs have been shown to significantly alter broader temperature and pressure patterns, disrupting critical climate systems like the El Niño-Southern Oscillation (ENSO) and the Indian summer monsoon (ISM) (1, 4, 5). The 1815 Mt. Tambora eruption, for instance, initiated a year-long global cooling phase, influencing monsoonal rainfall patterns and inducing enduring droughts, making it the largest TVE in recorded history (6).

The magnitude of the 1815 Mt. Tambora eruption, however, pales in comparison to that of another volcanic eruption that occurred in the Indonesian archipelago, around ~74 ka. Thought to be one of the largest volcanic eruptions in the last 23 million years (7), the eruption of Mount Toba on Sumatra discharged an estimated 5,300 km^3 of pyroclastic material, covering ~40 million km^2 with a layer of Younger Toba Tuff (YTT) exceeding 5 mm (7). The YTT super-eruption is estimated to have released at least 56 times more dense rock equivalent than the 1815 eruption at Mt. Tambora (7).

Drawing on ice and marine core records, genetic studies, and climate modeling, some researchers have proposed that the YTT eruption induced a 6-year-long global "volcanic winter" and even caused a human population bottleneck (8). Subsequent interdisciplinary investigations incorporating data from stalagmites, lacustrine and marine sediments, and paleontology have, however, proposed minimal environmental and global climatic impact (9). These observations are bolstered by sedimentary and archeological records demonstrating occupational continuity spanning the Toba eruption, particularly evident in Indian subcontinent where Middle Paleolithic (MP) technologies persist across YTT ash layers (10–14).

Most analyses of the YTT eruption to date have relied upon climate models and studies of vastly smaller historical eruptions (15) and have generally also lacked ground-truthing via proxy data (7). However, resolving debates about Toba's immediate impact necessitates high-resolution, on-the-ground investigation. Records of annual to decadal resolution offer an important means to assess Toba's immediate aftermath and effects on local ecosystems, but sedimentation rates, taphonomic changes and available chronometric methods have severely limited the availability, integrity, and utility of such records. Here, in order to assess Toba's immediate aftermath at a key YTT-yielding Paleolithic locality in southern India (see Fig. 1), we present new high-resolution, multiproxy paleoclimate data from the site of Jwalapuram (JWP) (10, 13). We undertake novel paleoenvironmental analysis of tephra deposits at JWP in order to investigate the annual-scale impact of the YTT eruption on human-inhabited ecosystems.

Study area

Situated on the southern flanks of the Jurreru River in Andhra Pradesh (Fig. 2), JWP is known for its well-preserved YTT deposits (Fig. 1) (10, 13, 16) and Paleolithic occupation record, ranging from ~77 ka to 11.3 ka (Fig. 1 and SI Fig. S2; Table S1) (17). Stratigraphically, the YTT layer rests on a reddish-brown palludal silty-clay deposit (layer D) and is capped by a yellow-brown ash mixed silty sand layer (layer B; see SI Table S1). The pre- and post-YTT deposits across the sites yielded significant evidence of hominin occupation, where pre-YTT MP occupations date back to ~74 ka (71 ± 8 ka) and 77 ka (17, 18). However, the revised age of layer A, containing post-YTT MP occupation, is around 35 ka to 38 ka, suggesting a sedimentary disconformity between layer A and layer B (18, 19). Nevertheless, the current work solely focuses on the YTT deposit, with the aim of understanding the immediate aftermath of the ~74 ka YTT eruption on the regional and local environment. The multilayer YTT deposit at JWP has been interpreted as a consequence of rapid YTT tephra deposition during ISM seasons immediately following the eruption (SI Fig. S1) (13, 16, 20). Successive monsoonal precipitation events after the YTT eruption are thought to have remobilized the unconsolidated tephra and concentrated it in valleys and topographically low-lying regions, likely by sheet wash and colluvial processes like slumping (SI Fig. S1) (13, 16). Lithostratigraphic data from JWP2020 reveals 2–3 m thick YTT tephra layers comprised of six sub-units of YTT horizons, interspersed by thin pale greyish-brown hardpan layers (Fig. 1; SI Figs. S1, S2, and S3; SI Table S1) (10, 13, 16, 17). Stratigraphic observations, including ripple and swirling marks, laminations, and upward fining of all tephra units, suggest deposition in an aqueous environment (SI Figs. S4 and S6; see SI Note S1 for more information on stratigraphy) (10, 13, 16, 17, 21). Additional features, such as mud cracks, burrowing, hardpan (dolocrete) formation, and the development of microbial mats, indicate desiccation and rapid drying following each wet period (Fig. 1; SI Figs. S11–S16) (16, 21). These stratigraphic features underscore oscillating wet-dry conditions, likely associated with annual monsoonal cyclicity (SI Figs. S17 and S18; see SI Note S2) (10, 13, 16, 21). While annually resolved chronometric data is beyond the capabilities of current methods, the stratigraphic evidence and existing sedimentological data coupled with new observations reported here indicates that the YTT ash deposits at JWP2020 likely represent six annual monsoonal cycles following the YTT super-eruption (10, 13, 16, 21), making JWP a rare terrestrial archive featuring exceptional temporal resolution in a Pleistocene context.

Results

Depositional history

Our work provides new chronological insights that complement earlier sedimentological data from the YTT deposits of JWP (10, 13, 16, 21). Scanning electron microscope (SEM) micrographs of tephra samples from the seven YTT layers (including a basal primary airfall tephra) show minimal alteration of glass shards, suggesting relatively rapid deposition of the tephra at JWP (SI Fig. S32). Elemental and mineralogical data indicate the geochemical similarity between primary YTT ash (SS6) and all redeposited tephra layers (SS5–SS0), suggesting no substantial mixing with nontephra material (Fig. 3 and SI Fig. S25). Principal component analysis (PCA) shows strong geochemical similarity within tephra layers, and a significant geochemical difference between the tephra and the nontephra layer (pre-YTT paleosol) (Fig. 3). The geochemical purity of all tephra units at JWP2020 suggests the rapid mobilization and deposition of YTT tephra during subsequent annual monsoonal seasons (Fig. 3, see SI Figs. S1 and S25).

The overall sinusoidal pattern of paleoprecipitation proxies (Rb/Sr and $\delta^{18}O_{PC}$) and paleovegetation proxies ($\delta^{13}C_{SOM}$ and

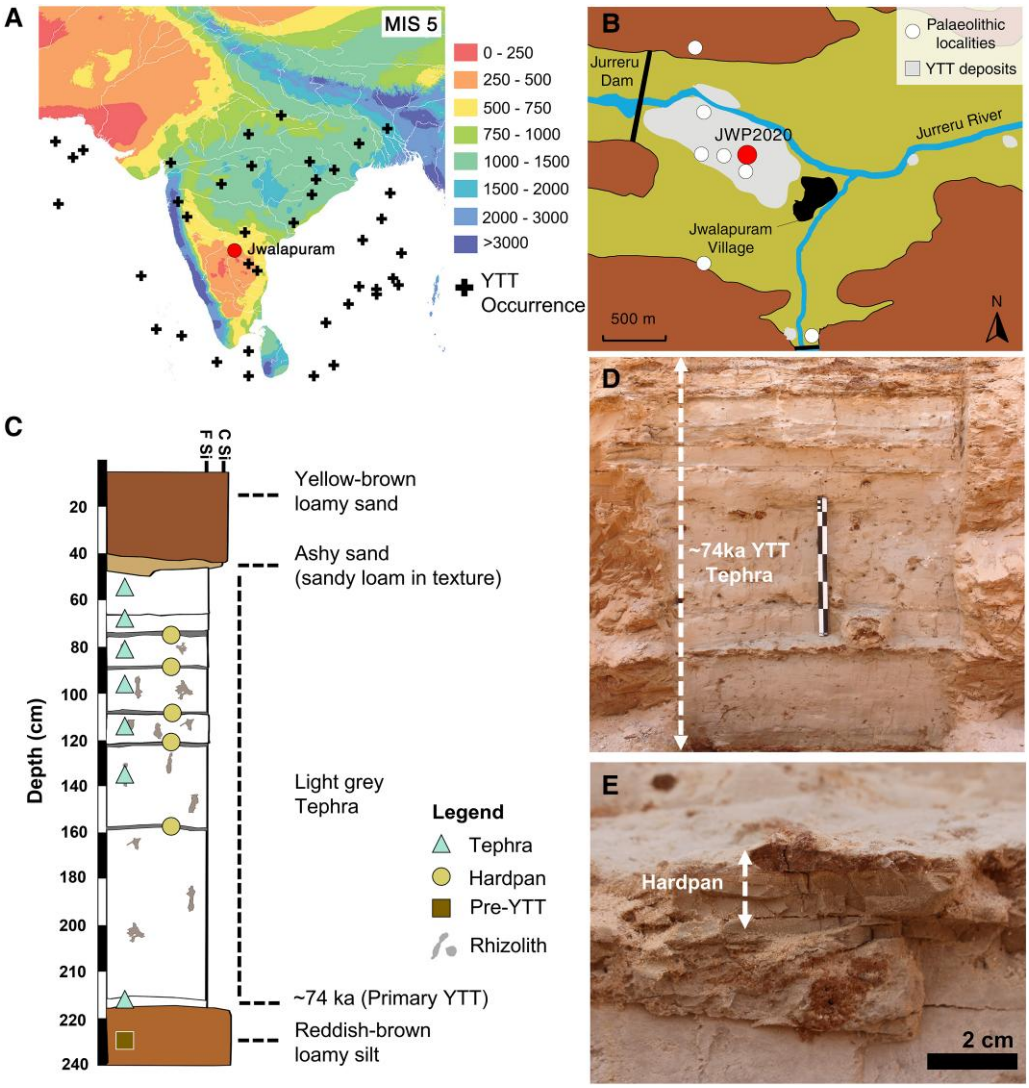

Fig. 1. A) Precipitation models showing of mean annual precipitation in the Indian subcontinent during marine isotope stage 5e; B) map showing the spatial distribution of Paleolithic sites and YTT tephra deposits in the Jurreru Valley, highlighting the location of JWP2020; C) lithostratigraphy of JWP2020 showing six to seven folds of YTT deposits demarcated by six layers of grayish hardpans; D) freshly exposed YTT tephra deposit at JWP; E) Close-up view of a greyish-brown hardpan layer. Legend: B) brown: hill ranges, green: alluvial plain, black: village, blue: water body; C) aqua blue: tephra/YTT sample, mustard: hardpan layer, and brown: pre-YTT sample; F Si: fine silt and C Si: coarse silt; E) scale: 1 unit = 10 cm. Base image courtesy: A) Based on the PMIP4 model, B) Modified after Jones et al. (13).

$\delta^{13}C_{PC}$) across the YTT JWP sequence mirror the pattern seen in the regional modern rainfall and temperature record from Andhra Pradesh (2009–2015; Fig. 2; SI Fig. S18) (22), illustrating the seasonal nature of climate fluctuation in the Pleistocene YTT tephra deposits at JWP, where tephra deposition represent wet ISM seasons and hardpan formation represents dry post-ISM seasons, forming an annual cycle. While we acknowledge that current chronometric methods cannot provide precise ages to support these assertions, recent and historical volcanic eruptions have shown depositional patterns similar to those at JWP (23–26), highlighting the seasonal reworking of tephra after the volcanic event, and leading to the formation of seasonally resolved inter-bedded tephra deposits in low-lying regions (e.g. lakes, ponds, and other topographic depressions).

Case studies worldwide reveal that rainfall onto fresh ash deposits rapidly mobilizes tephra through sheet wash, rill erosion, and aeolian activity, causing it to slump into low-lying areas like lakes and valleys, resulting in the formation of multiannual tephra laminations (refer to SI Note 2 for more information on chronology) (23, 27–29). A notable example is the YTT site at Kampung Luat 3 in Malaysia's Lenggong Valley, where Gatti et al. (20) identified two layers of Toba tephra at the site, each representing a rainy season, separated by hardpan layers marking dry seasons. Given that our data point to a depositional pattern similar to that seen for modern and recent volcanic events, our findings add further strong support to earlier arguments suggesting that the YTT sequence at JWP represents monsoonal cyclicity, spanning six annual cycles following the Toba super-eruption. In this case, each annual cycle comprised one wet (ISM = tephra mobilization) and one dry season (post-ISM = hardpan formation) (SI Figs. S1, S17, and S18; see SI Note S2 for more information on chronology).

One other line of evidence in support of our rapid chronological interpretation of the deposits concerns bioturbation patterns. The YTT tephra layers in the JWP sequence show a distinct bioturbation pattern compared to surrounding nontephra units, with

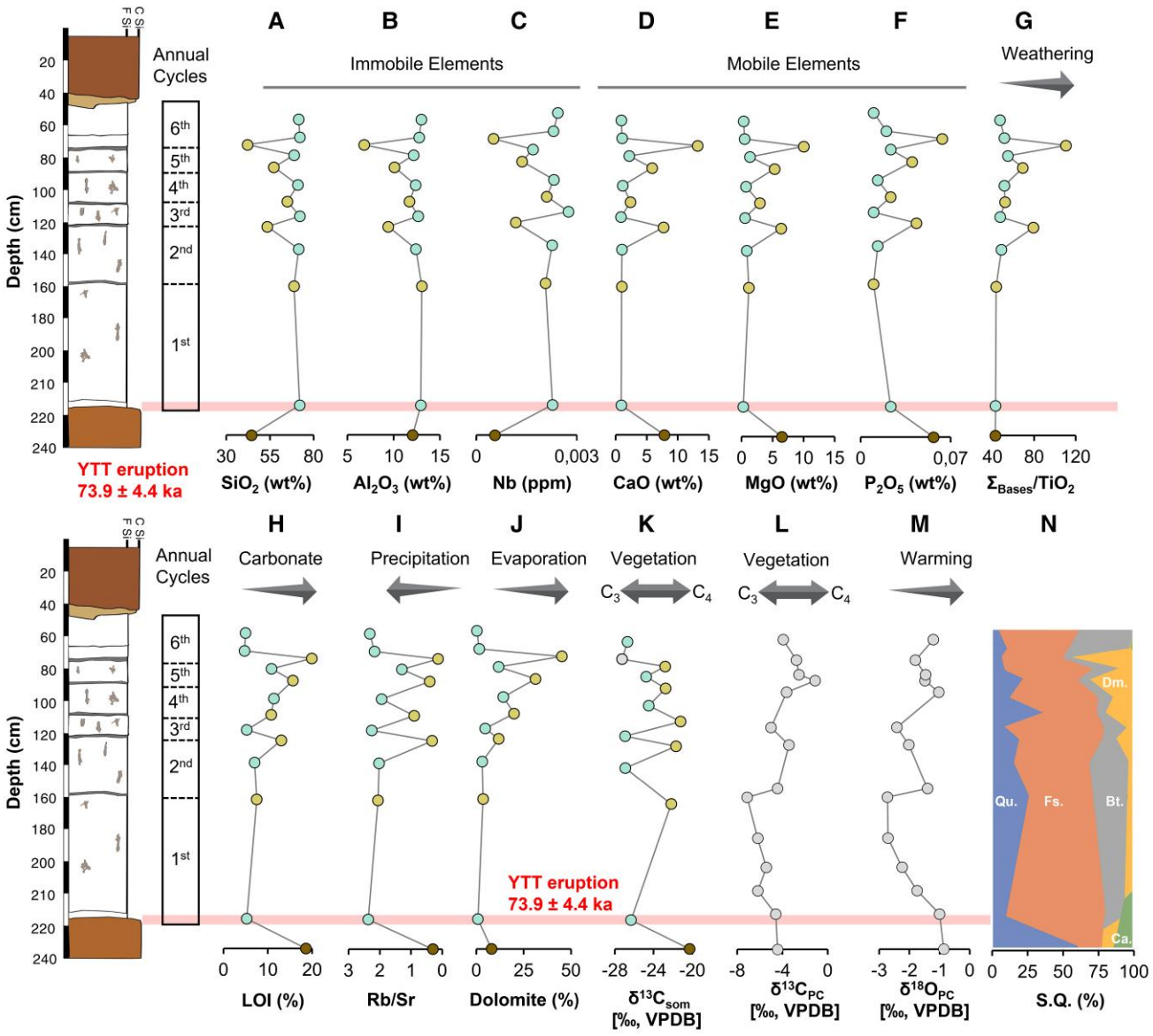

Fig. 2. Elemental concentrations (wt.%) of immobile elements—A) SiO_2, B) Al_2O_3, and C) Nb; elemental concentrations (wt.%) of mobile elements—D) CaO, E) MgO, and F) P_2O_5; G) leaching: ratio of bases to TiO_2; H) loss on ignition (carbonate %); I) ratio of Rubidium (Rb) to Strontium (Sr); J) Dolomite (%); K) Stable carbon isotope value of soil organic matter ($\delta^{13}C_{SOM}$); L) Stable carbon isotope values of pedogenic carbonate ($\delta^{13}C_{PC}$); M) oxygen isotope values of pedogenic carbonate ($\delta^{18}O_{PC}$); N) S.Q.% (relative concentrations) of different mineralogical groups—quartz (Qu.), feldspar (Fs.), biotite (Bt.), dolomite (Dm.), and clays (Ca.). Legend: brown: Pre-YTT layer, aqua blue: YTT/Tephra layers, and mustard: Hardpan; the red shaded line marks the primary YTT layer. Note: The bar graph indicating six annual cycles represents six monsoons following the YTT event; $\delta^{13}C_{PC}$ and $\delta^{18}O_{PC}$ dataset is taken from Haslam et al. (16). Refer to SI for complete geochemical data, proxy justification (SI Notes S3 and S4), and interpretation (SI Note S5).

significantly less extensive and diverse bioturbation (see SI Note S1 for more information of stratigraphic features). Burrowing in the YTT units is limited to simple, vertical shafts <1 cm in diameter, occasionally ending in small chambers, unlike the complex termite galleries in non-YTT units (SI Figs. S14 and S16). This suggests limited time for termitaria development before the next YTT deposition. Similarly, rhizoliths in the YTT units are less diverse, mainly consisting of weakly calcified rhizocretions, indicating limited plant colonization time (SI Figs. S10 and S13). Indications of a limited opportunity for bioturbation and plant colonization prior to the next tephra deposition episode imply a rapid sequence of events (30). These patterns suggest that the YTT at JWP was deposited quickly, likely during annual cycles, with rapid burial preserving local vegetation, as evidenced by in situ tree trunks and leaf imprints at different YTT localities in JWP (SI Figs. S7–S9; see SI note S1 for more information).

Elemental datasets

Pyroclastic materials (particularly silicate minerals) are subjected to postdepositional chemical weathering, providing insights into the nature of posteruptive environments, including water availability and temperature (31). The chemical weathering of freshly deposited volcanic tephra can occur at a rapid (annual) rate, primarily governed by regional climate conditions, particularly rainfall that plays a significant role as it provides the moisture

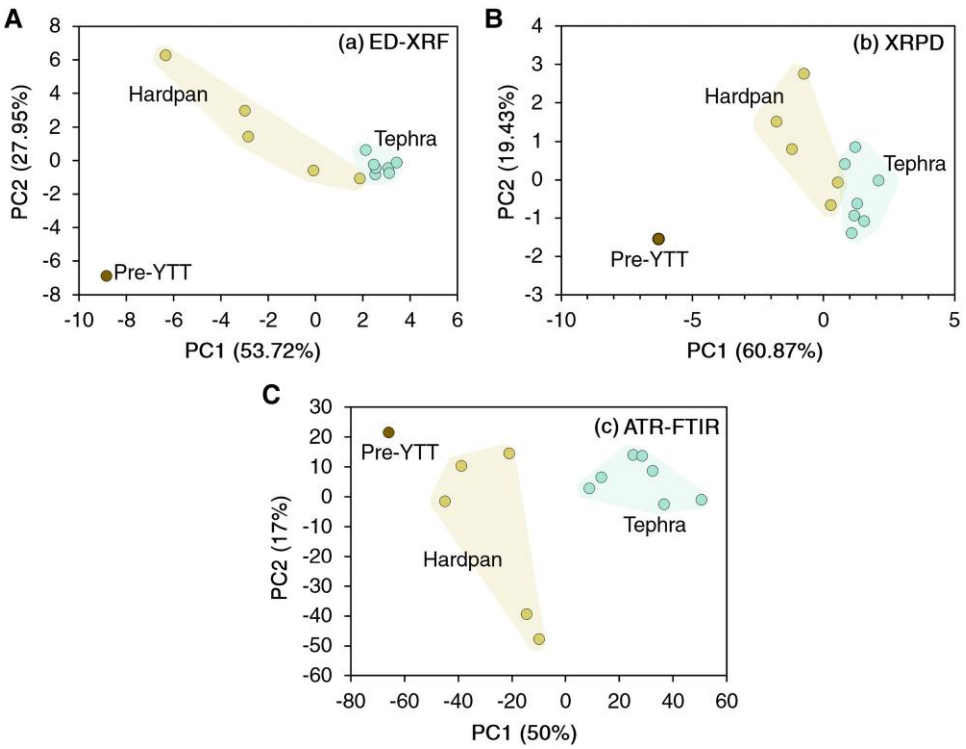

Fig. 3. PCA of ED-XRF (A), XRPD (B), and ATR-FTIR (C) datasets. PCA analysis of the XRF dataset indicates that the first two principal components (PC1 and PC2) of the elemental data account for 81.6% of the variance. PCA of all three datasets shows discrete clustering between YTT and Hardpan samples. Note: YTT and hardpan samples are geochemically distinct from the pre-YTT sample. Legend: brown: Pre-YTT layer, aqua blue: YTT/Tephra layers, and mustard: Hardpan; the red shaded line marks the primary YTT layer.

necessary for chemical reactions to occur (24, 31). The drainage conditions also affect how quickly tephra can weather, as well-drained areas (e.g. hill-slopes, river valleys, other high-gradient regions) may experience faster weathering due to rapid tephra mobilization during increased water movement (23, 26, 28). Additionally, the physical and chemical properties of the tephra itself, such as its mineral composition and the presence of mobile oxides (like—CaO and MgO), are critical in determining the rate and extent of weathering (see SI Notes S3 and S4 for more information) (26).

Tephra-derived silicate minerals show increasing hydrolysis under aqueous and subsequent evaporative conditions with increasing aridity (see SI Table S2) (26, 32) shaping concentrations of mobile and immobile elements (Figs. 2, 3, and 4; SI Figs. S19–S21) (33). Concentrations of immobile elements Al_2O_3, SiO_2, and TiO_2, across the YTT deposit show relatively uniform background values with a decrease in the hardpan layers (Fig. 2; SI Figs. S20 and S22). The average concentrations of major immobile elements—SiO_2, Al_2O_3, and TiO_2—were comparatively higher in tephra layers ($n = 7$; SiO_2: 71.33 ± 1.06 wt.%; Al_2O_3: 12.62 ± 0.28 wt.%; TiO_2: 0.14 ± 0.002 wt.%) relative to the hardpan layers ($n = 5$; SiO_2: 57.40 ± 9.28 wt.%; Al_2O_3:10.21 ± 2.12 wt.%; TiO_2: 0.17 ± 0.009 wt.%). The elemental mapping of hardpan samples confirms the distinct spatial distribution of elements, and indicates predominant concentration of Ca and Mg, along with lower levels of Al and Si, in hardpan layers relative to the tephra layers (Fig. 4). This difference in concentration was mirrored in trace elements such as Rb, Y, Zr, Nb, and Th (Fig. 2; SI Fig. S22). Hardpans on the other hand were enriched in alkali-earth base elements—CaO and MgO (Figs. 2 and 4; SI Fig. S21)—showing higher concentrations (CaO: 6.02 ± 4.31 wt.%; MgO: 5.15 ± 3.03 wt.%) compared to tephra layers (CaO: 1.14 ± 0.43 wt.% and MgO: 0.66 ± 0.33 wt.%). Other mobile elements such as S (0.018 ± 0.007 wt.%), P_2O_5 (0.036 ± 0.018 wt.%) and Sr (0.044 ± 0.028 ppm) also followed this pattern (Fig. 2; SI Fig. S21), with higher concentrations in hardpan layers and lower concentrations in tephra layers (S: 0.010 ± 0.001 wt.%, P_2O_5: 0.02 ± 0.01 wt.%, and Sr: 0.012 ± 0.002 ppm).

Lower chemical index of alteration (CIA <60), chemical index of weathering (<70), and plagioclase index of alteration (<60) values in hardpan layers indicate that they are primarily composed of early weathering products (SI Fig. S24; SI Table S3) (34). Molecular proxies of hydrolysis (Σ_{Bases}/Al_2O_3) and leaching (Σ_{Bases}/TiO_2) reflect mobility of base elements (primarily, CaO and MgO) relative to immobile elements like TiO_2 and Al_2O_3 (Fig. 3 and SI Fig. S22; SI Table S2) (28, 34). Both proxies showed relatively uniform background values for tephra layers (Σ_{Bases}/Al_2O_3: 0.53 ± 0.04; Σ_{Bases}/TiO_2: 49.06 ± 3.5) and pronounced increases in the hardpan horizons (Σ_{Bases}/Al_2O_3: 1.08 ± 0.6; Σ_{Bases}/TiO_2: 72.61 ± 26.39), likely related to the leaching of tephra-derived silicate minerals, and upward precipitation of base elements, leading to higher concentration of base cations in hardpan layers (32). Gradual reduction in concentration of base cations Ca^{2+} and Mg^{2+} in tephra layers and subsequent increase in hardpan layers suggests an initial stage of chemical alteration (28) (Fig. 2 and SI Fig. S25). Similar positive excursions in hardpan layers were also observed in Rb/Sr values, indicating enrichment of Sr in hardpans and Rb in tephra layers (Fig. 2). Here, we utilize Rb/Sr as a proxy for paleoprecipitation, as Rb mobility is strongly dependent on infiltration, whereas Sr is affected by evapotranspiration (see SI Note S4) (35). Rb/Sr ratios show a positive relationship ($R^2 = 0.89$; $P < 0.05$) with CIA-derived f_{diss} (feldspar dissolution) (36), showing positive excursions (i.e. increased water availability) in tephra layers (2.05 ± 0.3) and negative shifts (i.e. greater aridity) in the hardpan layers (0.76 ± 0.69) (SI Fig. S26).

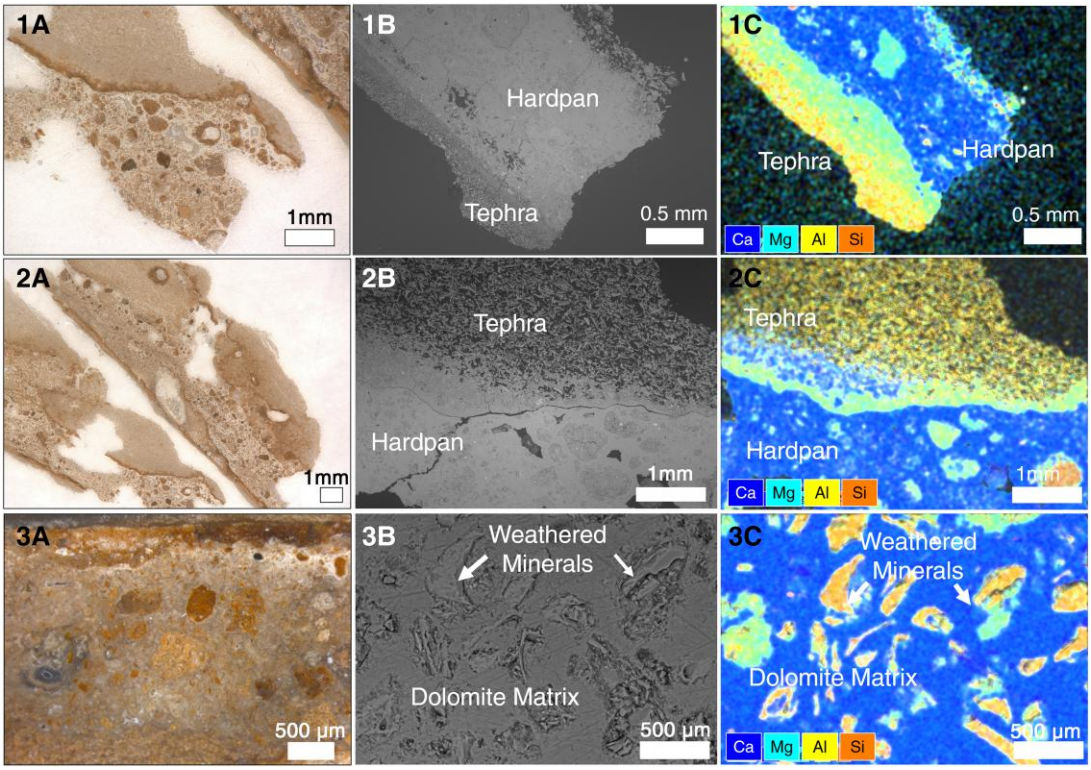

Fig. 4. 1A) and 2A) Thin-section of the YTT-hardpan interface; 1B) and 2B) SE micrograph showing cemented hardpan and unconsolidated tephra; 1C) and 2C) elemental map showing that the hardpan is primarily enriched in Ca and Mg, while the tephra is enriched in Al and Si; 3A) close-up picture of a hardpan fragment; 3B) SE micrograph showing weathered minerals embedded in a dolomite-enriched matrix; 3C) elemental map indicating a low concentration of Ca and Mg in leached glass shards and other silicate minerals. Color scheme for the elemental map—blue: calcium, arctic: magnesium, yellow: aluminum, and orange: silicon.

Mineralogical datasets

Changes in the mineralogical properties of bulk YTT tephra, which may have occurred due to chemical weathering after the YTT event, were also assessed. The mineralogical component of ultradistal tephra from the YTT eruption mainly consists of quartz, plagioclase, sanidine, biotite, amphibole, Fe–Ti oxides, orthopyroxene, allanite, fayalite, and zircon (37) (SI Figs. S27–S30). The dissolution of tephra-derived silicate minerals can occur rapidly, on a seasonal or annual basis, due to the high reactivity of volcanic glass and silicate minerals (feldspar and biotite in particular) in tephra (20, 38). This makes them susceptible to chemical weathering when exposed to water and varying environmental conditions (31). Seasonal changes, such as increased rainfall or temperature fluctuations, can further enhance the dissolution process by providing more water to facilitate chemical reactions (23, 28). This can lead to the rapid breakdown of silicate minerals like biotite and feldspar over shorter timescales (23, 26).

Here, we mainly focused on identifying major silicate and carbonate minerals in the JWP2020 tephra and hardpan deposits, such as quartz, plagioclase, sanidine, biotite, and dolomite (Fig. 2; SI Figs. S27–S30). Bulk ash was found to be predominantly composed of an amorphous glass fraction (83.9 ± 9.99%) with a varying crystalline fractions occurring across the JWP2020 sequence (SI Fig. S27). Tephra layers are rich in silicate minerals (plagioclase: 37.1 ± 8%; sanidine: 22 ± 2.3%; biotite: 23.8 ± 12.17%), while hardpans are predominantly (22.3 ± 14.6%) formed of dolomite (Fig. 2; SI Figs. S27, S29, and S30). We observed a strong link between loss of base (other mobile element) elements in underlying tephra and enrichment of same in capping hardpan layers, likely hinting towards the desiccation of tephra and subsequent formation of dolomitic hardpan (Fig. 2; SI Figs. S17, S29, and S30) (26, 28, 31).

Stable carbon isotope analysis and correlation matrices

JWP2020 soil organic carbon isotope ($\delta^{13}C_{SOM}$) values range from −20.3 to −27.2‰, indicating relatively uniform values fluctuating within the range expected for major contributions of C_3 plant biomass to the SOM (Fig. 2; see SI Note S4). We observed an oscillating trend across the JWP2020 sequence, whereby tephra layers (26.2 ± 1.0‰) present lower $\delta^{13}C_{SOM}$ values and hardpan layers (22.1 ± 0.6‰) have higher values. We observe an inverse relationship between total organic matter (TOM%) and $\delta^{13}C_{SOM}$, highlighting gradual decreases in the TOM of each hardpan in comparison to the underlying tephra layers (SI Fig. S19). Sinusoidal excursions in $\delta^{13}C_{SOM}$ values can be an indicator of change or variation in TOM influx, pCO_2 and vegetational stomatal response to seasonal wet-dry conditions (39). A similar distribution pattern has also been observed in the carbon and oxygen isotope analyses of pedogenic carbonate ($\delta^{13}C_{PC}$: 4.6 ± 1.6‰, and $\delta^{18}O_{PC}$ (1.9 ± 0.8‰) previously undertaken for the YTT unit of the JWP3 sequence (13) (Fig. 2).

Discussion

Contrary to the widely accepted notion of a prolonged volcanic cooling period triggered by the YTT eruption (8), our multiproxy paleoclimate data reveal a more nuanced scenario in the

terrestrial record of JWP. The first annual cycle is marked by the primary deposition of airfall tephra during a monsoonal season where airfall YTT was deposited in aqueous settings of JWP, indicating relatively wetter conditions in comparison to later seasons (13, 16). The first annual cycle demonstrated minimal mobility of base cations (Ca^{2+} and Mg^{2+}), characterized by a lower concentration of evaporite minerals (i.e. dolomite), and minimal chemical weathering of tephra. While the deposition and rapid mobilization of tephra in an aqueous environment may have potentially triggered hydrolysis and leaching of tephra-derived silicate minerals, the observed data reveals no significant mobility or upward precipitation of mobile elements, especially base cations, which is likely connected to the lack of evaporative conditions and suggests a lower surface temperature in compared to subsequent annual cycles (Fig. 2). Paleoclimate proxies, such as $\delta^{13}C_{SOM}$, $\delta^{13}C_{PC}$, Rb/Sr, and f_{diss}, showed minimal variation during the first annual cycle, further indicating relatively cooler conditions compared to subsequent cycles (Fig. 2) (28, 35). This interpretation is supported by the finding that the lowest dolomite and carbonate concentrations occur in the initial hardpan layer, signifying reduced evapotranspiration compared to later dry seasons when dolomite concentration increased successively (Fig. 2) (40, 41). While the YTT-induced volcanic cooling may have caused a negative temperature anomaly during the first annual cycle, our paleoclimate proxies indicate that such a cooling effect may have lasted only for 1 year (annual cycle) and was likely overshadowed by subsequent warming. These findings complement recent simulation work which documents uncertainties in the magnitude of Toba's sulphur emissions with high and low emission scenarios, and also supports a limited cooling impact ~74 ka on the Indian subcontinent (42).

After the first annual cycle, we observed initial signs of chemical weathering in the silicate minerals of the YTT tephra at JWP. This is indicated by a significant increase in the ratios of Σ_{Bases}/Al_2O_3 and Σ_{Bases}/TiO_2 during the second annual cycle (Fig. 2). The decreasing concentration of mobile elements in the second reworked tephra layer is likely related to increased hydrolysis and leaching of tephra-derived silicate minerals. This led to higher concentrations of mobile elements in the hardpans, along with elevated levels of dolomite and carbonates, suggesting strong warming and evaporation following a moderate first annual cycle (26, 28, 31). The third annual cycle showed similar fluctuations, with wetter conditions during tephra deposition, as evidenced by increased Rb/Sr ratios and concentrations of immobile elements (Fig. 2). This cycle was followed by a dry period, marked by a rise in mobile elements and more intense chemical weathering compared to the previous tephra layer (Fig. 2). However, the dolomite and carbonate levels were lower than in the second hardpan, indicating milder conditions than the second annual cycle (Fig. 2). We observe that the third hardpan (end of third annual cycle) marked the start of a multiannual increase in the concentration of CaO, MgO, P_2O_5, S, and Sr in the hardpan layers, which indicates progressing chemical weathering of tephra-derived silicate minerals and increase in mobility in such elements (Fig. 2; SI Fig. S20) (26, 43, 44). The higher dissolution of tephra-derived feldspar and biotite, and an increase in the concentration of dolomite in hardpan, likely relates to a progressive chemical weathering and strengthening of evaporative conditions after annual season (26, 28, 31). Trends of dolomite concentration and silicate mineral dissolution show a step-wise increase, confirming a gradual temperature rise (26, 28, 31, 44), a trend also reflected in $\delta^{18}O_{PC}$ and $\delta^{13}C_{PC}$ records (13), which point to warming and intensifying aridity (Fig. 2; SI Figs. S30 and S31) (13). This warming trend is inversely reflected in Rb/Sr measurements, showing a decrease in rainfall, leading to strong arid conditions during the second to fifth annual cycle (Fig. 2) (28, 35). This warming phase peaked during the formation of the fifth and last hardpan layer, potentially causing significant disruption to regional ecologies.

We suggest that the approximate 4-year warming phase after the first annual cycle reflects YTT's influence on ENSO dynamics (1–5), leading to a multiannual El Niño event that may have weakened the ISM and caused drought across the region (1, 4, 5). The YTT eruption may have perturbed interhemispheric and land–sea thermal contrasts, resulting in a southward movement of the intertropical convergence zone and weakening of the ISM (1, 4, 5). Strong coupling of ISM and ENSO dynamics, due to the weakening of monsoon Hadley circulation and the low-level monsoon jet, could have led to drier conditions and reduced moisture transport from the Indian Ocean towards the Indian subcontinent, causing enhanced surface warming (1, 4, 5). It is important to note that the JWP sequence does not present direct evidence for ENSO-ISM changes. Nonetheless, multiple, smaller-scale TVEs in the last two centuries show significant impacts of volcanic forcing on ENSO-ISM patterns, resulting in a precipitation deficit due to weakening of the ISM linked to post-TVE El-Nino warming (2–5).

Drawing parallels with the 4-year (1991–1995) long period of warming and low-rainfall following the 1991 Mt. Pinatubo eruption helps to provide context for understanding the potential effects of YTT-induced climatic change in India (SI Fig. S33; refer to SI Note S6 for more info). The weakening of the ISM for 4 years led to severe drought conditions in India, causing water scarcity and vegetation loss (4) (SI Fig. S33). India also witnessed an increase in forest fire incidents in summer 1995 (45), likely related to the peak of the warming phase. The intensity of the post-YTT warming period would have depended on the volcano's sulphate load and its impact on the Indian ocean dipole (5, 42), highlighting the need for further research into the potential factors behind a post-YTT warming phase.

After the formation of the last hardpan layer at JWP (MS5), we observe a dramatic reduction in weathering indices, molecular ratios of hydrolysis-leaching, and the concentrations of mobile elements, as well as a marked decrease in the concentration of dolomite and decrease in $\delta^{13}C_{SOM}$, suggesting the diminishing impact of the warming phase and environmental recovery (Fig. 2). Phytolith analysis supports this conclusion, with the appearance of grass morphotypes indicating a return of vegetation in the local landscape (13). The last YTT ash redeposition phase is followed by the deposition of orange pedogenically altered ash-rich silty sand, marking the first episode of sedimentation after the YTT event (Fig. 1; SI Figs. S2 and S3) (13, 16). Increased non-ash sediment load and higher magnetic susceptibility likely indicate landscape stabilization after eruption-induced perturbation (SI Fig. S19) (16). These signatures of rapid environmental resurgence after YTT deposition at JWP agree with recent climate model data (42), suggesting a muted impact of the YTT event on India. Overall, we find evidence for an initial year of muted cooling following the eruption, followed by a multiyear warming period, and then a year of environmental stabilization.

Conclusions

Our study provides the first direct, on-site proxy data to reconstruct the immediate, local environmental impact of the ~74 ka Toba super-eruption at a key hominin-inhabited site in the peninsular Indian subcontinent. Our novel palaeoclimate data do not

show any signs of a "volcanic winter." Instead, they present a contrasting scenario in the immediate aftermath of the eruption. Here, we interpret patterns of tephra weathering (SI Fig. S25) and dolomite enrichment (SI Fig. S31) as indicators of warming and aridity after YTT, likely linked to weakening of the ISM and regional warming (Fig. 2; SI Fig. S17; see SI Note S5 for detailed synthesis). While a couple years of warming and drying would have had adverse effects on local ecologies, near-extinction events seem unlikely, and diverse environmental responses across the Indian subcontinent can be expected (16, 46, 47). It is important to highlight the limitations of the current dataset, particularly concerning spatial insights into palaeoclimate variability. Factors such as biogeographical setting, volume of ash, nature of local hydrology, and topography would have played critical roles in driving regional variability in YTT impacts (16, 46). Furthermore, diverse ecological settings across the Indian subcontinent would have provided interconnected mosaic habitats and relatively stable precipitation, facilitating faunal mobility and reduced the likelihood of climate-induced-extinctions (46, 48). Archeological research in India indicates continuity of Middle Paleolithic populations and no significant changes in technological practices over the period 74–56 ka, consistent with persistent hominin presence across the subcontinent spanning the ~74 ka Toba super-eruption (10–12, 17, 49, 50). Our high-resolution multiproxy paleoclimate data from JWP offer novel first-hand evidence concerning the short-term impact of YTT in a distal terrestrial setting away from the Toba caldera, providing a key geographic reference point for generating more nuanced insights into the impacts of the super-eruption on regional and global climates and environments. We suggest that our multiproxy palaeoclimate approach can be effectively applied to other highly resolved terrestrial tephra records, to provide valuable insights into the regional impacts of significant historical volcanic eruptions, such as the ~40 ka Campanian Ignimbrite event and the 25.3 ka Dawson event, on past climate and ecosystems. Furthermore, to avoid simplistic and sometimes deterministic conclusions regarding the impact of global geological events such as volcanic eruptions, these effects must be assessed via on-site proxy data, with an aim to provide nuanced understanding on human–climate–environment relationships.

Materials and methods

Sample collection and prescreening

The current study focuses specifically on the Toba (YTT) ash layer (Layer C) and its six sub-units (C1 to C6) at JWP2020 (refer to SI Fig. S2). JWP2020 is a newly exposed YTT-bearing section located adjacent to the well-known archeological site of JWP3. Both sites share a similar stratigraphy, featuring a six-layered YTT tephra horizon (see SI Figs. S2 and S3). To prevent modern contamination, we excavated a small geological test trench (50 cm × 50 cm × 250 cm) to remove the outermost surface and expose the underlying horizon (SI Fig. S3). Each YTT sub-unit consists of two components: tephra and hardpan. Representative samples were collected from each YTT sub-unit, comprising seven tephra samples (SS6–SS0) and five hardpan samples (MS1–MS5) (see SI Note S1). The primary objective of this study was to investigate the geochemistry of the different tephra and hardpan layers, with the aim of understanding the climatic context of tephra deposition and hardpan formation at JWP. Additionally, one sediment sample (nontephra material) was collected from unit D to analyze the geochemistry of the local sediment deposit.

Collected sediment samples were dried in a Memmart oven at 40 °C for 24 h. All samples were screened under a LEICA M205C stereomicroscope and a Hirox digital microscope (HRX-01) at the HERCULES Laboratory, Évora, Portugal. The primary intent was to study signs of physical alteration and other biogenic features, particularly in the hardpan samples. Samples were homogenized using an agate mortar and pestle for geochemical analyses.

Energy dispersive-X-ray fluorescence

Major and minor elemental compositions of the bulk sediment samples ($N = 13$) were obtained using a Bruker S2 Puma energy dispersive X-ray spectrometer (EDS-XRF) equipped with a silver anode X-ray tube at HERCULES Laboratory, Évora, Portugal. The concentrations of elements were quantified with SPECTRA. LOADER software uses a regression method to obtain a calibration curve of 27 siliceous standard reference materials. Each sample was analyzed three times to estimate the standard deviation in elemental concentration (see SI Geochemical dataset). The samples were analyzed as fused discs using Li-tetraborate flux with a flux:sample ratio of 10:1. A Claisse Fluxer LeNeo TM fusion instrument performed the fusion. The loss of ignition (LOI) was evaluated by calcination (on crucibles) of 1 g of dry sample in a muffle furnace for 1 h at 1,050 °C. LOI allows quantification of the loss that occurred during fused bead formation. LOI values are also crucial paleoclimatic proxies indicating complete water loss in tephra layers.

Scanning electron microscopy-energy dispersive spectroscopy

Bulk YTT ($n = 6$) and Hardpan fragments ($n = 5$) were analyzed using a variable pressure SEM (Hitachi S3700N) coupled to an EDS-XRF (Bruker Xflash 5010SDD) at the HERCULES Laboratory Évora, Portugal. The samples were analyzed at an accelerating voltage of 20 kV and at a low vacuum (40 Pa). Samples were placed on the carbon-tape-coated sample holder and images were acquired in the secondary electron (SE) mode. Some of the samples were sputtered with gold to create a conductive surface. Samples were sputtered using a 25 mA sputter current for 120 s in a Q150R Plus—Rotary Pumped Coater.

Apart from raw samples, resin-impregnated hardpan thin sections ($n = 2$) were analyzed for elemental characterization. Multiple spot/point (single and multiple), line, and basic mapping were performed. The operating conditions for EDS analysis were as follows: backscattering mode, 20 kV accelerating voltage, 10 mm working distance, 100 μA emission current, and 40 Pa pressure in the chamber.

X-ray powder diffraction

X-ray powder diffraction (XRPD) was employed for mineralogical characterization, determining the impact of paleopedological processes on the crystalline structure of different mineralogical compounds. Finely powdered samples ($n = 13$) were assessed by XRPD using a Bruker AXS D8 Discover XRD with the Da Vinci design at the HERCULES Laboratory, Évora, Portugal. A Cu Kα source operating at 40 kV and 40 mA and a Lynxeye 1D detector were used. Scans were run from 3 to 75° 2θ, with 0.05 2θ step and 1 s/step measuring time. Hardpan samples ($n = 5$) were reassessed for finer compound segregation, ran at 14 s per step with 0.02° increment. Diffract-EVA software with the PDF-2 mineralogical database (International Centre for Diffraction Data) was utilized to interpret XRPD patterns. This software also enabled the determination of the crystalline and amorphous fractions of all samples, and the semiquantitative (S.Q.) analysis of the diffraction data.

Attenuated total reflection–Fourier transform infrared spectroscopy

Bulk sediment samples ($n = 13$) were screened using an attenuated total reflection–Fourier transform infrared spectroscopy (ATR-FTIR). Multiple infrared (IR) spectra were produced using a Bruker ALPHA FTIR spectrometer at the HERCULES Laboratory, Évora, Portugal. ∼0.5 g of homogenized sample was placed over the ATR crystal plate. The results were acquired in absorption mode. Spectra were collected using OPUS 7.2 software with a spectral resolution of 4 cm^{-1} and 32 scans. Produced IR spectra was corrected using extended ATR correction in the OPUS program. Further, baseline correction and normalization were also performed. Exported IR data were processed in Microsoft Excel and ORIGIN software, where diagnostic IR peaks (like CO_3) were statistically quantified using Gaussian correlations.

Elemental analyzer isotope ratio mass spectrometry

Bulk sediment samples ($n = 13$) were analyzed for stable carbon isotope (soil organic matter) analysis. For decarbonization, 5 g of homogenized samples was suspended in 2 M HCL for 24 h. Decarbonized samples are further rinsed with milli-Q water to neutralize the pH. Treated samples were dried at 40 °C for 24 h and rehomogenized. ∼40 μg of each sample (along with their duplicates) were packed into tin capsules and measured for total organic carbon (TOC) and $\delta^{13}C$ values in a Thermo Scientific Isotope Ratio Mass Spectrometer coupled with a Thermo Scientific FLASH 2000 HT Elemental Analyzer via ConFlo IV at the stable isotope laboratory of the Max Planck Institute of Geoanthropology, Jena, Germany. USGS61, IAEA-C6, IAEA-N2, USGS40, and IAEA-Urea were used as standards for calibration and TOC (%) measurement. All the $\delta^{13}C$ values are reported in Vienna Peedee Belemnite scale.

Statistical analysis of geochemical data

Two-tailed t test

The current study uses a two-tailed t test to determine if there is a significant difference between the means of two groups of data (i.e. comparison between different geochemical proxies). In the context of current geochemical data, a two-tailed t test provides insights into whether there is a substantial difference between the means of two sets of elemental or mineralogical data or observations. The in-built data analysis feature of Microsoft Excel was used for this analysis.

Pearson correlation coefficient

The Pearson correlation coefficient (r) quantifies the strength and direction of a linear relationship between two geochemical variables (i.e. correlation between different geochemical proxies), providing insights into how two geochemical variables are related. A Pearson correlation coefficient matrix was prepared to measure the linear correlation between different paleoclimatic proxies. The R program was used to do this analysis.

PCA of ED-XRF. XRPD and ATR-FTIR datasets

PCA was performed to explore complex geochemical datasets, identifying patterns, reducing dimensionality for visualization, and uncovering relationships among geochemical variables. The variables were normalized and mean-centered before computing the principle components. The R program was used for this analysis.

Acknowledgments

We would like to thank the Archaeological Survey of India for permission to conduct fieldwork in the Kadapa basin and adjoining region. We would also like to thank the HERCULES laboratory of the University of Évora (Portugal), the Maharaja Sayajirao University of Baroda (India), and the Max Planck Institute of Geoanthropology (Germany) for facilitating this research. G.J. and D.A. thank Zakir Khan and the villagers of Jwalapuram for their help during field sampling. G.J. would like to thank Dr. Anne-France Maurer, Dr. Luís Dias, Dr. Margarida Padeira Nunes, Dr. Sriradha Bhattacharya, Dr. Ana Cardoso, Dr. Ana Zélia Miller, and Dr. Nicasio Tomás Jiménez-Morillo for their help during lab work at HERCULES Laboratory, Évora, Portugal. G.J. also thanks Dr. Jana Ilgner, Mary Lucas, and Erin Scott for supporting lab work at the Max Planck Institute of Geoanthropology. G.J. also thanks Dr. Tejasvi Chauhan for valuable discussion on volcano-climate teleconnections. M.C. would like to acknowledge projects UIDB/04449/2020 and UIDP/04449/2020 (DOI:10.54499/UIDB/04449/2020 and 10.54499/UIDP/04449/2020), and the IN2PAST project (LA/P/0132/2020), all of which are funded by the Fundação para a Ciência e a Tecnologia. Financial support for the current research was provided by EMJMD ARCHMAT (based at University of Évora, Portugal) and the Max Planck Institute of Geoanthropology, Jena, Germany.

Supplementary Material

Supplementary material is available at *PNAS Nexus* online.

Funding

This project is funded by EMJMD ARCHMAT program and Max Planck Gesellschaft (MPG).

Author Contributions

G.J. designed the study. G.J., K.K., D.A., and R.R.J. conducted the fieldwork. G.J., A.T., M.C., C.D., S.S., and P.R. conducted geochemical analysis of soil/tephra samples and produced geochemical dataset. G.J., C.D., M.C., S.B., O.W., J.L., D.J., P.R., and R.R.D. worked on curation of geochemical dataset. P.D. and G.J. reassessed the older geoarchaeological and sedimentological dataset. G.J. wrote the article, and M.P., N.B., P.R., S.B., O.W., P.D., J.L., D.J., R.R.D., H.A., R.R.J., K.K., D.A., C.D., M.C., A.T., and R.P. edited the article. Visuals are produced and edited by G.J., R.P., S.B., O.W., S.S., and R.R.D.

Data Availability

All data are included in the manuscript and/or supporting information.

References

1 Zhuo Z, Kirchner I, Pfahl S, Cubasch U. 2021. Climate impact of volcanic eruptions: the sensitivity to eruption season and latitude in MPI-ESM ensemble experiments. *Atmos Chem Phys*. 21: 13425–13442.

2 Freychet N, Schurer AP, Ballinger AP, Suarez-Gutierrez L, Timmreck C. 2023. Assessing the impact of very large volcanic eruptions on the risk of extreme climate events. *Environ Res*. 2: 035015.

3 Dogar MM, *et al.* 2023. A review of El Niño southern oscillation linkage to strong volcanic eruptions and post-volcanic winter warming. *Earth Syst Environ.* 7:15–42.
4 Fadnavis S, *et al.* 2021. The role of tropical volcanic eruptions in exacerbating Indian droughts. *Sci Rep*. 11:2714.
5 Singh M, *et al.* 2020. Fingerprint of volcanic forcing on the ENSO-Indian monsoon coupling. *Sci Adv*. 6:eaba8164.
6 Wilson N, *et al.* 2023. Impact of the Tambora volcanic eruption of 1815 on islands and relevance to future sunlight-blocking catastrophes. *Sci Rep*. 13:3649.
7 Costa A, Smith VC, Macedonio G, Matthews NE. 2014. The magnitude and impact of the Youngest Toba Tuff super-eruption. *Front Earth Sci (Lausanne)*. 2:1–8.
8 Ambrose SH. 1998. Late Pleistocene human population bottlenecks, volcanic winter, and differentiation of modern humans. *J Hum Evol*. 34:623–651.
9 Ge Y, Gao X. 2020. Understanding the overestimated impact of the Toba volcanic super-eruption on global environments and ancient hominins. *Quat Int*. 559:24–33.
10 Petraglia M, *et al.* 2007. Middle paleolithic assemblages from the Indian subcontinent before and after the Toba super-eruption. *Science (1979)*. 317:114–116.
11 D. Anil, *et al.* 2023. Youngest Toba Tuff deposits in the Gundlakamma River basin, Andhra Pradesh, India and their role in evaluating Late Pleistocene behavioral change in South Asia. *Quat Res*. 115:134–145. https://doi.org/10.1017/qua.2023.13
12 Clarkson C, *et al.* 2020. Human occupation of northern India spans the Toba super-eruption ~74,000 years ago. *Nat Commun*. 11:961.
13 Haslam M, *et al.* 2010. The 74 ka Toba super-eruption and southern Indian hominins: archaeology, lithic technology and environments at Jwalapuram locality 3. *J Archaeol Sci*. 37:3370–3384.
14 Anil D, *et al.* 2024. Deep-rooted Indian Middle Palaeolithic: terminal Middle Pleistocene lithic assemblage from Retlapalle, Andhra Pradesh, India. *PLoS One*. 19:e0302580.
15 Williams M. 2012. The ~73 ka Toba super-eruption and its impact: history of a debate. *Quat Int*. 258:19–29.
16 Jones SC. 2010. Palaeoenvironmental response to the ~74 ka Toba ash-fall in the Jurreru and Middle Son valleys in southern and north-central India. *Quat Res*. 73:336–350.
17 Petraglia MD, Ditchfield P, Jones S, Korisettar R, Pal JN. 2012. The Toba volcanic super-eruption, environmental change, and hominin occupation history in India over the last 140,000 years. *Quat Int*. 258:119–134.
18 Haslam M, *et al.* 2012. A southern Indian Middle Palaeolithic occupation surface sealed by the 74 ka Toba eruption: further evidence from Jwalapuram locality 22. *Quat Int*. 258:148–164.
19 Funaki T, *et al.* 2022. New chronometric dating of Indian Middle/Upper Palaeolithic sites at Jwalapuram, Andhra Pradesh, Southern India. *J Archaeol Stud India*. 2:101–113.
20 Gatti E, *et al.* 2013. Depositional processes of reworked tephra from the Late Pleistocene Youngest Toba Tuff deposits in the Lenggong Valley, Malaysia. *Quat Res (United States)*. 79:228–241.
21 Oppenheimer C. *Eruptions that shook the world* Cambridge University Press, 2011.
22 O. Kwiecien, *et al.* 2022. What we talk about when we talk about seasonality—a transdisciplinary review. *Earth Sci Rev*. 225:103843.
23 Bolós X, Macias JL, Ocampo-Díaz YZE, Tinoco C. 2021. Implications of reworking processes on tephra distribution during volcanic eruptions: the case of Parícutin (1943–1952, western Mexico). *Earth Surf Process Landf*. 46:3143–3157.
24 Collins BD, Dunne T. 2019. Thirty years of tephra erosion following the 1980 eruption of Mount St. Helens. *Earth Surf Process Landf*. 44:2780–2793.
25 Froese DG, Zazula GD, Reyes AV. 2006. Seasonality of the late Pleistocene Dawson tephra and exceptional preservation of a buried riparian surface in central Yukon Territory, Canada. *Quat Sci Rev*. 25:1542–1551.
26 Fiantis D, Nelson M, Shamshuddin J, Goh TB, Van Ranst E. 2010. Leaching experiments in recent tephra deposits from Talang volcano (West Sumatra), Indonesia. *Geoderma*. 156:161–172.
27 Óskarsson BV, Riishuus MS, Arnalds Ó. 2012. Climate-dependent chemical weathering of volcanic soils in Iceland. *Geoderma*. 189–190:635–651.
28 Fiantis D, Nelson M, Shamshuddin J, Goh TB, Van Ranst E. 2010. Determination of the geochemical weathering indices and trace elements content of new volcanic ash deposits from Mt. Talang (West Sumatra) Indonesia. *Eurasia Soil Sci*. 43:1477–1485.
29 Kirkbride MP, Dugmore AJ. 2003. Glaciological response to distal tephra fallout from the 1947 eruption of Hekla, south Iceland. *J Glaciol*. 49:420–428.
30 Klappa CF. 1980. Rhizoliths in terrestrial carbonates: classification, recognition, genesis and significance. *Sedimentology*. 27:613–629.
31 Bonatotzky T, Ottner F, Erlendsson E, Gísladóttir G. 2021. Weathering of tephra and the formation of pedogenic minerals in young Andosols, South East Iceland. *Catena (Amst)*. 198:105030.
32 Fiantis D, Nelson M, Van Ranst E, Shamshuddin J, Qafoku NP. 2009. Chemical weathering of new pyroclastic deposits from Mt. Merapi (Java), Indonesia. *J Mt Sci*. 6:240–254.
33 Sheldon ND, Tabor NJ. 2009. Quantitative paleoenvironmental and paleoclimatic reconstruction using paleosols. *Earth Sci Rev*. 95:1–52.
34 Price JR, Velbel MA. 2003. Chemical weathering indices applied to weathering profiles developed on heterogeneous felsic metamorphic parent rocks. *Chem Geol*. 202:397–416.
35 Ouyang C, *et al.* 2019. The Rb/Sr ratio response to paleo precipitation recorded by lake sediment from a semi closed lake in southwest China since 16.0 cal. ka BP. *Ekoloji Dergisi*. 107:3901–3912.
36 Williams JZ, Bandstra JZ, Pollard D, Brantley SL. 2010. The temperature dependence of feldspar dissolution determined using a coupled weathering-climate model for Holocene-aged loess soils. *Geoderma*. 156:11–19.
37 Chesner CA. 2012. The Toba Caldera Complex. *Quat Int*. 258:5–18.
38 Krishnan G, Achyuthan H. 2019. Incipient weathering of the ~74ka Young Toba Tuff (YTT) biotite grains, Sagileru Valley, Andhra Pradesh. *J Geol Soc India*. 94:573–578.
39 Kirkels FMSA, *et al.* 2022. Carbon isotopic ratios of modern C3 and C4 vegetation on the Indian peninsula and changes along the plant-soil-river continuum—implications for vegetation reconstructions. *Biogeosciences*. 19:4107–4127.
40 Achyuthan H, Shankar N, Braida M, Ahmad SM. 2012. Geochemistry of calcretes (calcic palaeosols and hardpan), Coimbatore, Southern India: formation and paleoenvironment. *Quat Int*. 265:155–169.
41 Kaczmarek SE, Gregg JM, Bish DL, Machel HG, Fouke BW. 2017. Dolomite, very high-magnesium calcite, and microbes—implications for the microbial model of dolomitization. *SEPM Spec Publ*. 109:7–20.
42 Black BA, Lamarque JF, Marsh DR, Schmidt A, Bardeen CG. 2021. Global climate disruption and regional climate shelters after the Toba supereruption. *Proc Natl Acad Sci U S A*. 118:1–8.

43 Bünemann EK, Condron LM. 2007. Phosphorus and sulphur cycling in terrestrial ecosystems. *Nutr Cycling Terr Ecosyst*. 10:65–92.
44 Srivastava AK, Singh A, Sharma N, Khare N. 2020. Weathering pattern of Youngest Toba Tuff, Purna alluvial basin, Central India. *Arabian J Geosci*. 13:1–12.
45 Parashar A, Biswas S. 2003. The impact of forest fire on forest biodiversity in the Indian Himalayas (Uttaranchal). In: *XII World forestry congress*. Vol. 58. Dehradun: Forest Research Institute. p. 54.
46 Roberts P, Blinkhorn J, Petraglia MD. 2018. A transect of environmental variability across South Asia and its influence on Late Pleistocene human innovation and occupation. *J Quat Sci*. 33: 285–299.
47 Jha DK, Sanyal P, Philippe A. 2020. Multi-proxy evidence of Late Quaternary climate and vegetational history of north-central India: implication for the Paleolithic to Neolithic phases. *Quat Sci Rev*. 229:106121.
48 Roberts P, *et al*. 2014. Continuity of mammalian fauna over the last 200,000 y in the Indian subcontinent. *Proc Natl Acad Sci U S A*. 111:5848–5853. DOI 10.1073/pnas.1323465111
49 Jha G, Sinha DK, Jha DK, Ajithprasad P. 2024. Coasting into India? -Assessing lithostratigraphic context of Middle Palaeolithic occupation in Saurashtra Peninsula. *Quat Environ Humans*. 2:100034.
50 Jha G, Kothari V, Vyas V, Ajithprasad P. 2023. Assessing systematic blade production in the Indian Subcontinent with special reference to Eastern Gujarat. *Quaternary*. 6:25.